SUPPLEMENTAL MATERIAL

for the manuscript by

Takashi Daiho, Stefania Danko, Kazuo Yamasaki, and Hiroshi Suzuki

Stable Structural Analog of Ca^{2+}-ATPase ADP-insensitive Phosphoenzyme with Occluded Ca^{2+} Formed by Elongation of A-domain/M1'-linker and Beryllium Fluoride Binding

Supplemental Figure S1.

Mn^{2+} dependence of the rate of *E*P inhibition by BeF_x in 0.01 mM Ca^{2+}.

In *A*, microsomes expressing the mutant 4Gi-46/47 were incubated for various periods with BeF_x (1 mM KF plus 10 μM $BeSO_4$) in 0.01 mM $CaCl_2$ and various concentrations of $MnCl_2$ in the absence of $MgCl_2$ otherwise as in Fig. 6. The samples were then diluted and phosphorylated with 10 μM [γ-^{32}P]ATP and the amount of *E*P formed was determined as in Fig. 6. *Solid lines* show the least squares fit to a single exponential. In *B*, the rate constants obtained in *A* were plotted versus the concentration of Mn^{2+} added. $K_{0.5}$ for the Mn^{2+} activation and Hill coefficient obtained by fitting to the Hill equation (*solid line*) were 1.4 mM and 2.1, respectively.

Fig. S1

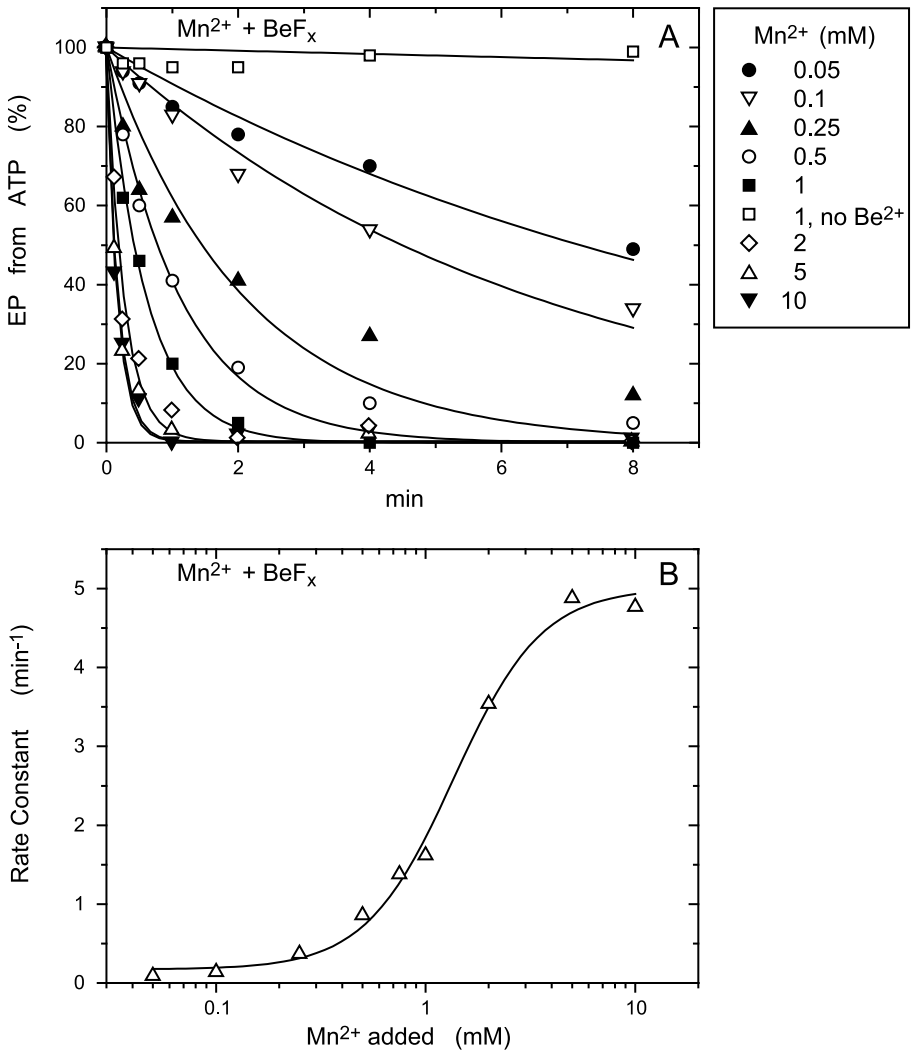

Supplemental Figure S2.

Ca^{2+} dependence of the rate of *E*P inhibition by BeF_x in the absence of Mg^{2+} and Mn^{2+}.

In *A*, microsomes expressing the mutant 4Gi-46/47 were incubated for various periods with BeF_x (1 mM KF plus 10 μM $BeSO_4$) and various concentrations of $CaCl_2$ in the absence of $MgCl_2$ otherwise as in Fig. 7. The samples were then diluted 10-fold and phosphorylated with 10 μM [γ-^{32}P]ATP and the amount of *E*P formed was determined as in Fig. 7. *Solid lines* show the least squares fit to a single exponential. In *B*, the rate constants obtained in *A* were plotted versus the concentration of Ca^{2+} added. $K_{0.5}$ for the Ca^{2+} activation and Hill coefficient obtained by fitting to the Hill equation (*solid line*) were 0.76 mM and 1.7, respectively.

Fig. S2

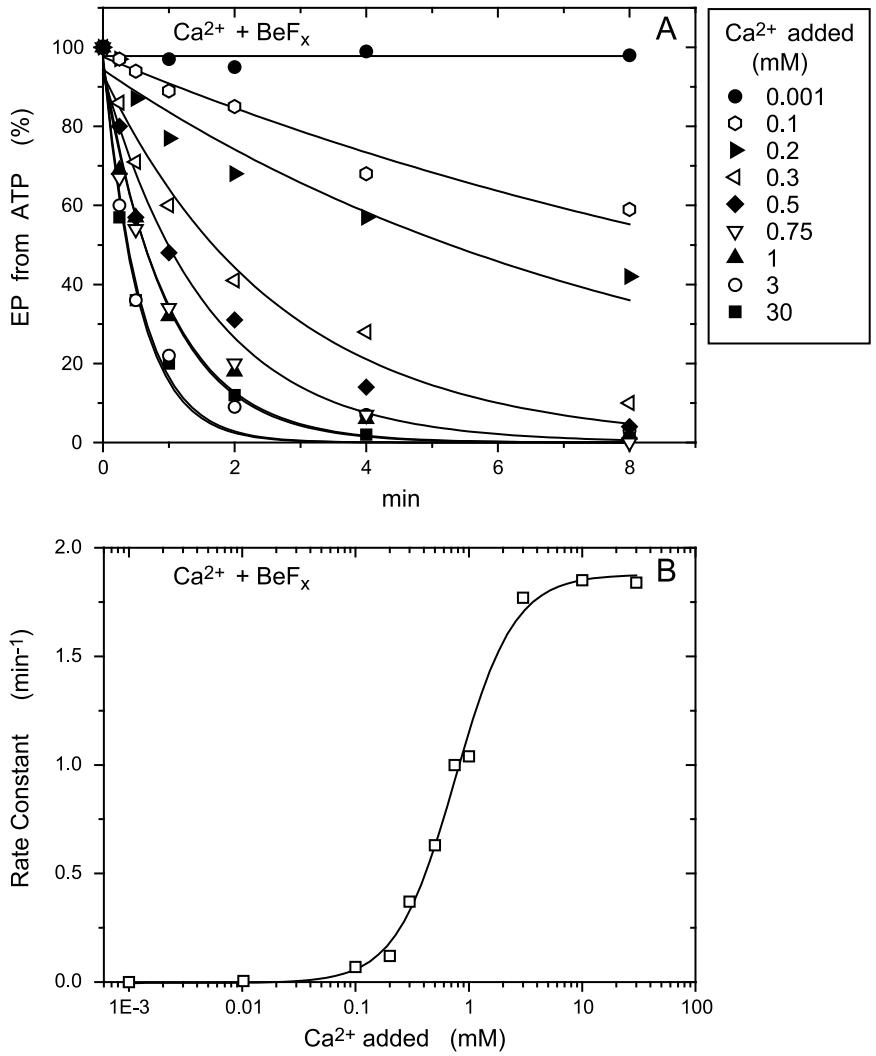

Supplemental Figure S3.

Proteolysis of the major intermediates and Ca^{2+}-ATPase complexes with metal fluoride in Ca^{2+}.

The major intermediates and their structural analogs were produced with the wild type and mutant 4Gi-46/47 in the microsomes (0.15 mg/ml) under the following conditions, and subjected to the limited proteolysis with 0.5 mg/ml trypsin (*A*, *B*) or prtK (*C*, *D*) at 25 °C and then to SDS-PAGE with the immunodetection as described in "EXPERIMENTAL PROCEDURES".

The *E*2 and *E*1Ca_2 states were formed in 1 mM EGTA and in 0.01 mM $CaCl_2$, respectively, in 15 mM $MgCl_2$, 1 μM A23187, 0.1 M KCl, and 50 mM MOPS/Tris (pH 7).

To produce *E*P from ATP, the microsomes were incubated at 25 °C for 10 s in 0.5 mM ATP, 10 mM $CaCl_2$, 15 mM $MgCl_2$, 1 μM A23187, 0.1 M KCl, and 50 mM MOPS/Tris (pH 7.0). In the wild type, *E*P accumulated was exclusively *E*1PCa_2·Ca (ADP-sensitive *E*P with the occluded two Ca^{2+} and with bound Ca^{2+} at the catalytic Mg^{2+} site), and its isomerization (therefore decay) was extremely slowed due to the Ca^{2+} ligation at the catalytic Mg^{2+} site and the feedback inhibition by the high concentration of lumenal Ca^{2+}. In the mutant, *E*P accumulated was exclusively *E*2PCa_2·Ca (ADP-insensitive *E*P with the occluded two Ca^{2+} and with bound Ca^{2+} at the catalytic Mg^{2+} site), and its decay was almost completely blocked due to the elongation of the A/M1'-linker (14).

To produce *E*1Ca_2·AlF_x, the microsomes were incubated at 25 °C for 30 min in 0.01 mM $CaCl_2$, 1 mM KF, 50 μM $AlCl_3$, 15 mM $MgCl_2$, 0.1 M KCl, and 50 mM MOPS/Tris (pH 7.0). For the *E*1Ca_2·AlF_4^-·ADP formation, the microsomes were further incubated for 10 min with 0.5 mM ADP.

The BeF_x treatment of the microsomes was performed in 0.01 mM $CaCl_2$, 1 mM KF, 50 μM $BeSO_4$, 0.1 M KCl, and 50 mM MOPS/Tris (pH 7) in the presence of 15 mM $MgCl_2$, or in place of $MgCl_2$, 10 mM $CaCl_2$ or 1 mM $MnCl_2$ as indicated in the figure. The wild type produced the *E*1PCa_2 analog *E*1Ca_2·BeF_3^- with Mg^{2+} and Mn^{2+} but not with Ca^{2+} (27), and the mutant produced the *E*2PCa_2 analog *E*2Ca_2·BeF_3^- with Mg^{2+}, Mn^{2+}, and Ca^{2+}.

The tryptic T1 site is very rapidly cleaved producing the fragments "A" (Met^1-Arg^{505}, immunodetected) and "B" (Ala^{506} to the C-terminus Gly^{994}, not immunodetected). Further cleavage at T2 site (Arg^{198}) produces the fragments "A1" (Ala^{199} to Arg^{505}, immunodetected) and "A2" (Met^1 to Arg^{198}, not immunodetected). The fragments formed by prtK are "p95" (Lys^{120}-Gly^{994}), "p81" (Met^1-Met^{733}), and "p83" (Glu^{243}-Gly^{994}) (all immunodetected) (54, 55). The digestion periods and the positions of the Ca^{2+}-ATPase, its fragments, and the molecular mass markers (kDa) are indicated. Note that the antibody unexpectedly immunodecorated trypsin (*A*, *B*) as previously observed (14). PrtK was also immunodecorated by the antibody against the Ca^{2+}-ATPase (*C*, *D*) as noted previously (14), but this band at the bottom of gels seems to include small ATPase fragments in addition to prtK since the rapid ATPase digestion is apparently associated with the more intense immunodecoration. In *A* and *B*, a band was sometimes observed after 4 min digestion and whose mass is intermediate (roughly ~60 kDa) between those of native ATPase and the "A" fragment. In the literature, such a fragment has never been observed in the tryptic digestion of the SR Ca^{2+}-ATPase, *i.e.* the rapid cleavage at T1 site (Arg^{505}) always occurs first producing the "A" and "B" fragments, whose migration rates are virtually the same in this SDS-PAGE system (*e.g.* see Refs. 23, 24). Therefore, the ~60-kDa band may possibly be due to non-specific immunodecoration of some fragment of contaminating protein (of which mass before cleavage is possibly similar to the 110 kDa-ATPase chain) in the microsome preparation.

Cleavage and resistance at the major sites Arg^{198}, Leu^{119}, and Thr^{242} are summarized in supplemental Table S1, and the results are described below in "***Proteolytic Structural Analysis of E2Ca_2·BeF_3^- (E2PCa_2) and Other Intermediates Formed from E1Ca_2***".

Supplemental Figure S4.

Proteolysis of the Ca^{2+}-ATPase complexes with metal fluoride formed without Ca^{2+} and treated with subsequently added Ca^{2+}.

Ca^{2+}-free *E*2·BeF_3^-, *E*2·AlF_4^-, and *E*2·MgF_4^{2-} were produced with the microsomes (0.15 mg/ml) in 1 mM EGTA, 1 mM KF, 1 μM A23187, and 50 mM MOPS/Tris (pH 7) by the incubation at 25 °C for 30 min in 50 μM $BeSO_4$, 7 mM $MgCl_2$, and 50 mM LiCl (*E*2·BeF_3^-); 50 μM $AlCl_3$, 1 mM $MgCl_2$, and 0.1 M KCl (*E*2·AlF_4^-); and 5 mM $MgCl_2$ and 0.1 M KCl (*E*2·MgF_4^{2-}). These complexes were further incubated with and without the addition of 10 mM Ca^{2+} at 25 °C for 30 min, and subjected to proteolysis with trypsin (*A*, *B*) or prtK (*C*, *D*), SDS-PAGE, and immunodetection as in Supplemental Fig. S3. Cleavage and resistance at Arg^{198}, Leu^{119}, and Thr^{242} are summarized in supplemental Table S2, and the results are described below in "***Proteolytic Structural Analysis of E2Ca_2·BeF_3^- Formed from E2·BeF_3^- and Ca^{2+}***".

Fig. S3A,B

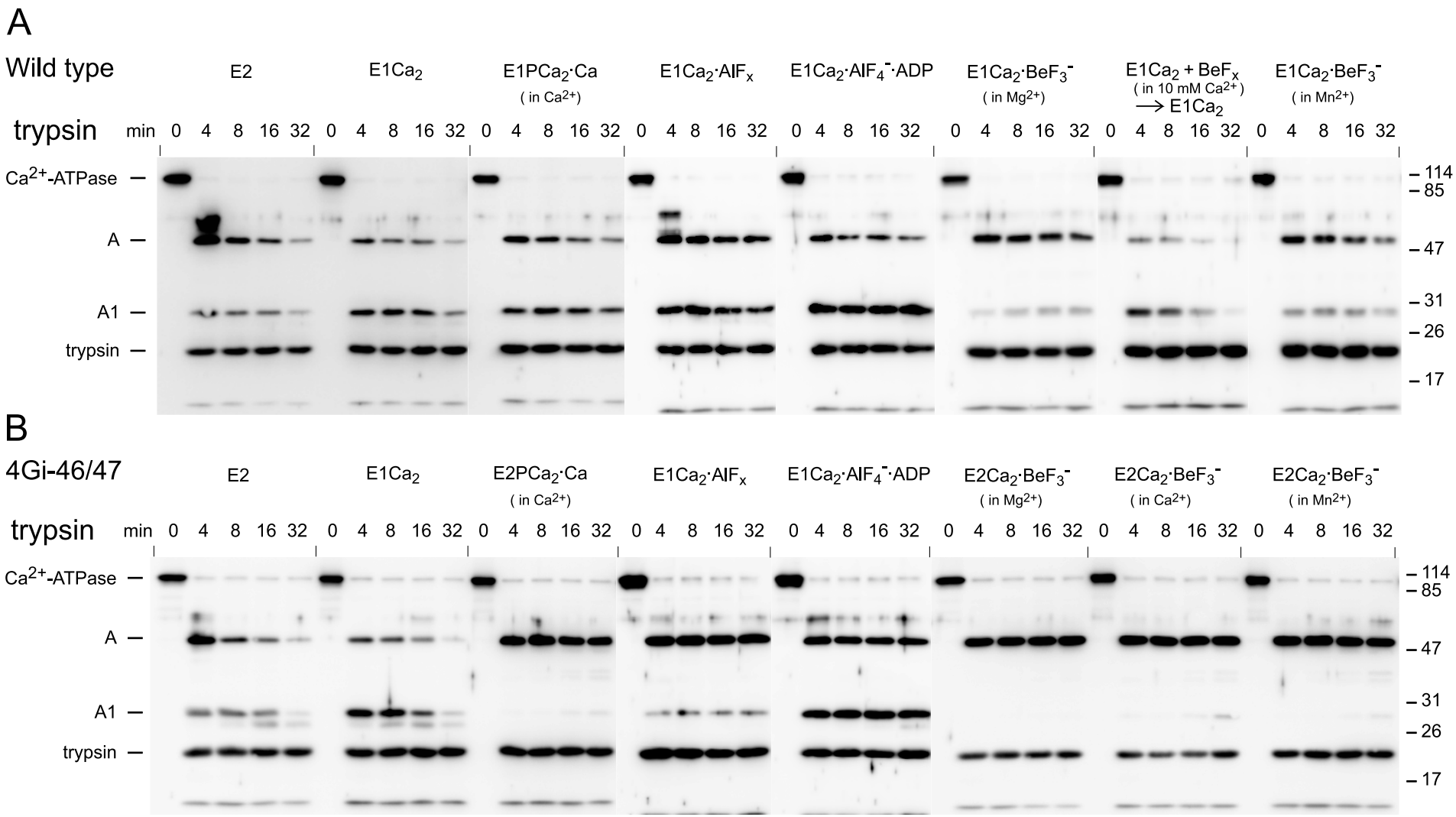
A
Wild type
E2
E1Ca2
E1PCa2·Ca
(in Ca2+)
E1Ca2·AlFx
E1Ca2·AlF4-·ADP
E1Ca2·BeF3-
(in Mg2+)
E1Ca2 + BeFx
(in 10 mM Ca2+)
→ E1Ca2
E1Ca2·BeF3-
(in Mn2+)
trypsin
min 0 4 8 16 32
Ca2+-ATPase
A
A1
trypsin
114
85
47
31
26
17
B
4Gi-46/47
E2
E1Ca2
E2PCa2·Ca
(in Ca2+)
E1Ca2·AlFx
E1Ca2·AlF4-·ADP
E2Ca2·BeF3-
(in Mg2+)
E2Ca2·BeF3-
(in Ca2+)
E2Ca2·BeF3-
(in Mn2+)
trypsin
min 0 4 8 16 32
Ca2+-ATPase
A
A1
trypsin
114
85
47
31
26
17

Fig. S3C,D

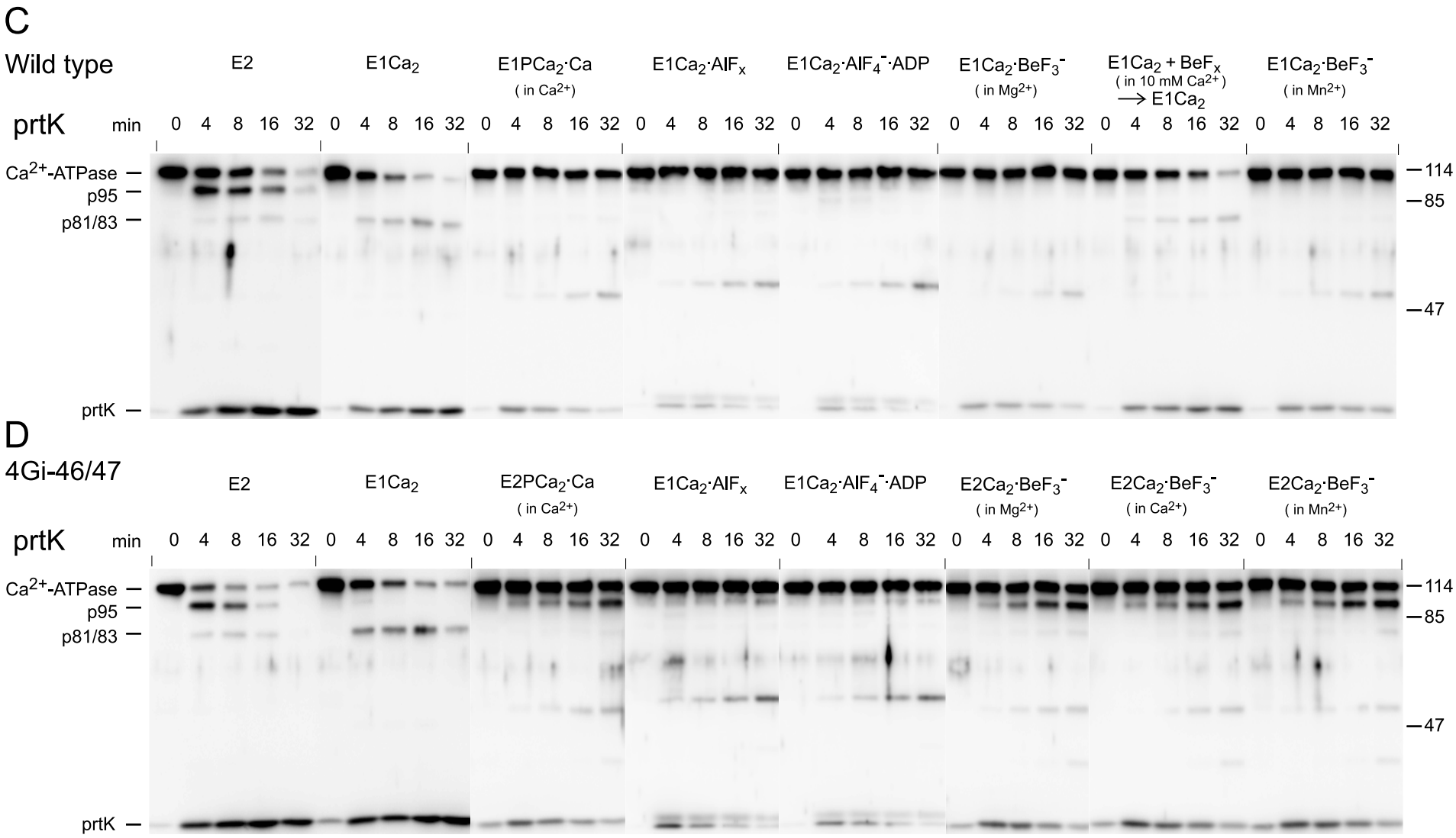
C
Wild type
E2
E1Ca2
E1PCa2·Ca
(in Ca2+)
E1Ca2·AlFx
E1Ca2·AlF4-·ADP
E1Ca2·BeF3-
(in Mg2+)
E1Ca2 + BeFx
(in 10 mM Ca2+)
→ E1Ca2
E1Ca2·BeF3-
(in Mn2+)
prtK
min
0 4 8 16 32
Ca2+-ATPase
p95
p81/83
prtK
114
85
47
D
4Gi-46/47
E2
E1Ca2
E2PCa2·Ca
(in Ca2+)
E1Ca2·AlFx
E1Ca2·AlF4-·ADP
E2Ca2·BeF3-
(in Mg2+)
E2Ca2·BeF3-
(in Ca2+)
E2Ca2·BeF3-
(in Mn2+)
prtK
min
0 4 8 16 32
Ca2+-ATPase
p95
p81/83
prtK
114
85
47

Fig. S4A,B

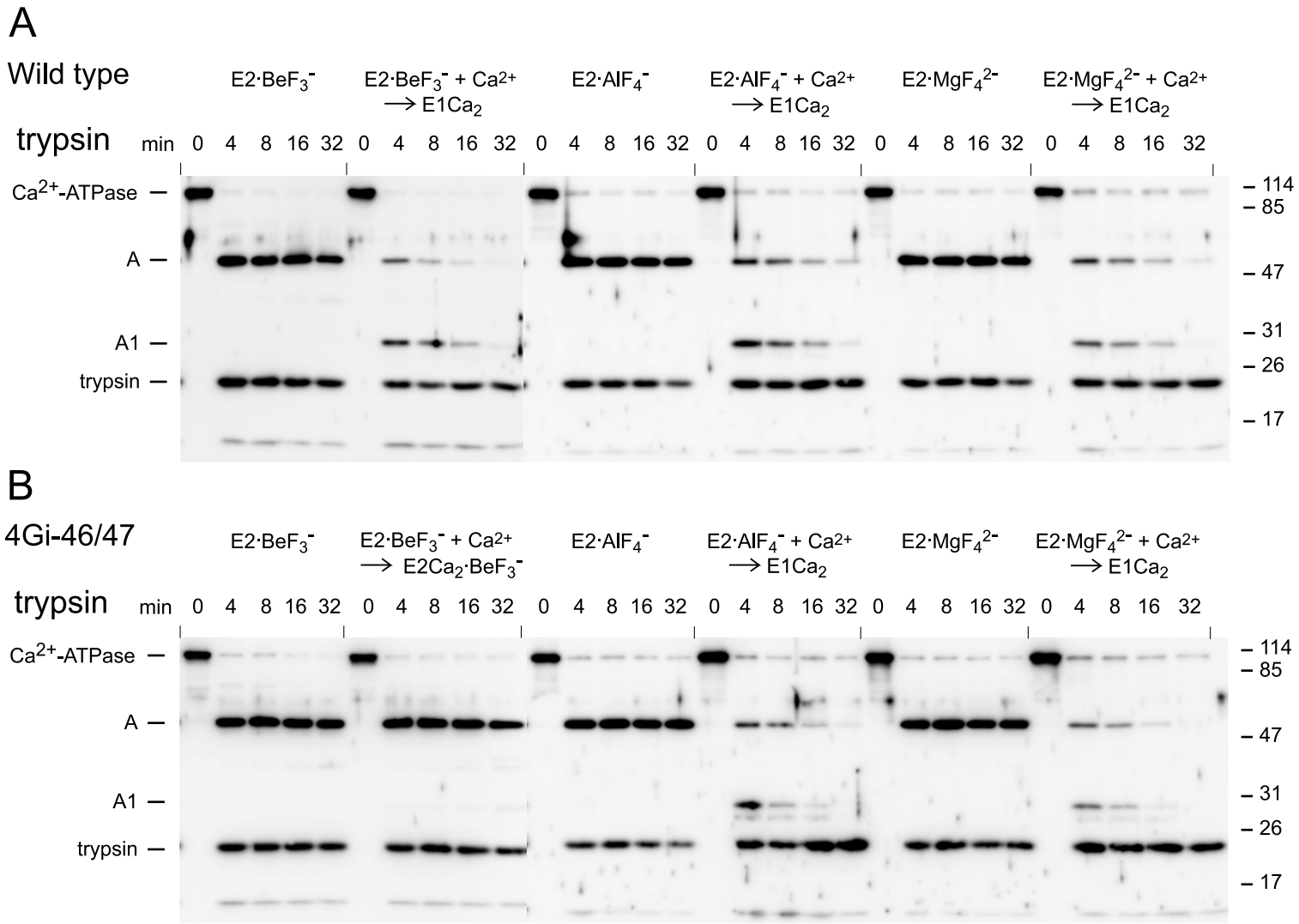
A
Wild type
E2·BeF3-
E2·BeF3- + Ca2+ → E1Ca2
E2·AlF4-
E2·AlF4- + Ca2+ → E1Ca2
E2·MgF42-
E2·MgF42- + Ca2+ → E1Ca2
trypsin
min 0 4 8 16 32 0 4 8 16 32 0 4 8 16 32 0 4 8 16 32 0 4 8 16 32 0 4 8 16 32
Ca2+-ATPase
A
A1
trypsin
114
85
47
31
26
17
B
4Gi-46/47
E2·BeF3-
E2·BeF3- + Ca2+ → E2Ca2·BeF3-
E2·AlF4-
E2·AlF4- + Ca2+ → E1Ca2
E2·MgF42-
E2·MgF42- + Ca2+ → E1Ca2
trypsin
min 0 4 8 16 32 0 4 8 16 32 0 4 8 16 32 0 4 8 16 32 0 4 8 16 32 0 4 8 16 32
Ca2+-ATPase
A
A1
trypsin
114
85
47
31
26
17

Fig. S4C,D

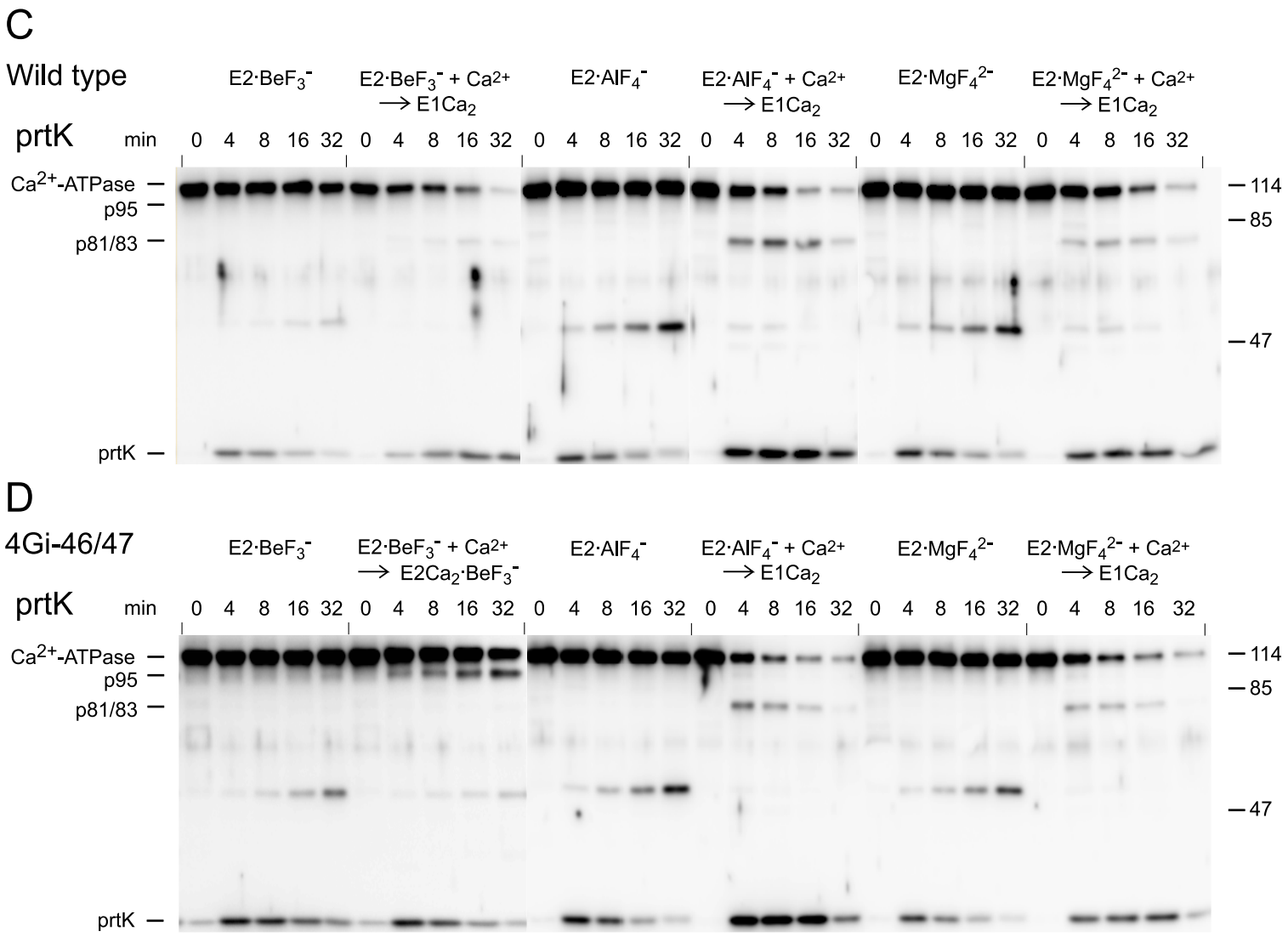
C
Wild type
E2·BeF3-
E2·BeF3- + Ca2+ → E1Ca2
E2·AlF4-
E2·AlF4- + Ca2+ → E1Ca2
E2·MgF42-
E2·MgF42- + Ca2+ → E1Ca2
prtK
min
0 4 8 16 32 0 4 8 16 32 0 4 8 16 32 0 4 8 16 32 0 4 8 16 32 0 4 8 16 32
Ca2+-ATPase
p95
p81/83
prtK
114
85
47
D
4Gi-46/47
E2·BeF3-
E2·BeF3- + Ca2+ → E2Ca2·BeF3-
E2·AlF4-
E2·AlF4- + Ca2+ → E1Ca2
E2·MgF42-
E2·MgF42- + Ca2+ → E1Ca2
prtK
min
0 4 8 16 32 0 4 8 16 32 0 4 8 16 32 0 4 8 16 32 0 4 8 16 32 0 4 8 16 32
Ca2+-ATPase
p95
p81/83
prtK
114
85
47

Supplemental Table S1

Summary of proteolysis of the major intermediates and their analogs in supplemental Fig. S3.
Relative cleavage rates of the tryptic T2 site (Arg^{198}) and prtK sites (Leu^{119} and Thr^{242}), and the complete resistance against the proteases were classified as follows by the visual inspection of the band intensities (A1, p95, and p81/83, respectively) in supplemental Fig. S3. The result for $E2{\cdot}BeF_3^-$ (in Mg^{2+}) in supplemental Fig. S4 was also included.

(+++) cleaved rapidly
(++) cleaved at moderate rate
(+) cleaved slowly
(—) completely resistant

Cleavage site		$E2$ →	$E1Ca_2$ →	$E1Ca_2{\cdot}AlF_4^-{\cdot}ADP$ ~	$E1Ca_2{\cdot}AlF_x$ →	$E1PCa_2$ $E1Ca_2{\cdot}BeF_3^-$ (in Mg^{2+} or Mn^{2+}) →	$E2PCa_2$ $E2Ca_2{\cdot}BeF_3^-$ (in Mg^{2+}, Mn^{2+}, or Ca^{2+}) →	$E2P$ $E2{\cdot}BeF_3^-$ (in Mg^{2+})
Arg^{198} (tryptic T2) producing "A1"	Wild type	+++	+++	+++	+++	+	No accumulation	—
	4Gi-46/47	+++	+++	+++	++	No accumulation	—	—
Leu^{119} (prtK) producing "p95"	Wild type	+++	—	—	—	—	No accumulation	—
	4Gi-46/47	+++	—	—	—	No accumulation	++	—
Thr^{242} (prtK) producing "p81/83"	Wild type	++	++	—	—	—	No accumulation	—
	4Gi-46/47	++	+++	—	—	No accumulation	—	—

Supplemental Table S2

Summary of proteolysis of $E2{\cdot}BeF_3^-$, $E2{\cdot}AlF_4^-$, and $E2{\cdot}MgF_4^{2-}$ with and without treatment by 10 mM Ca^{2+} in A23187 in supplemental Fig. S4.
Relative cleavage rates and the complete resistance were classified with the band intensities in supplemental Table S1.
(+++) cleaved rapidly
(++) cleaved at moderate rate
(+) cleaved slowly
(−) completely resistant

Cleavage site		$E2P$	+10 mM Ca^{2+}	$E2PCa_2$			+10 mM Ca^{2+}			+10 mM Ca^{2+}		+10 mM Ca^{2+}	
		$E2{\cdot}BeF_3^-$	→	$E2Ca_2{\cdot}BeF_3^-$	→	$E1Ca_2{\cdot}BeF_3^-$	→	$E1Ca_2$	$E2{\cdot}AlF_4^-$	→	$E1Ca_2$	$E2{\cdot}MgF_4^{2-}$	→	$E1Ca_2$
Arg^{198} (tryptic T2) producing "A1"	Wild type	−		No accumulation		No accumulation		+++	−		+++	−		+++
	4Gi-46/47	−		−		No accumulation		No accumulation	−		+++	−		+++
Leu^{119} (prtK) producing "p95"	Wild type	−		No accumulation		No accumulation		−	−		−	−		−
	4Gi-46/47	−		+++		No accumulation		No accumulation	−		−	−		−
Thr^{242} (prtK) producing "p81/83"	Wild type	−		No accumulation		No accumulation		++	−		+++	−		++
	4Gi-46/47	−		−		No accumulation		No accumulation	−		+++	−		++

Proteolytic Structural Analysis of $E2Ca_2{\cdot}BeF_3^-$ ($E2PCa_2$) and Other Intermediates Formed from $E1Ca_2$ — for supplemental Fig. S3 and Table S1 —

Strategy :

In *E*P isomerization and Ca^{2+} release ($E1PCa_2 \rightarrow E2P + 2Ca^{2+}$), the A domain substantially rotates and comes above one half of the P domain, and these domains incline significantly towards M2, which also inclines (see Fig. 2). In the resulting *E*2P, the A domain is associated with the P domain through interaction networks at the $TGES^{184}$ loop with the Asp^{351} region and at the Val^{200} loop with the polar residues of the P domain. In *E*2P, the A and P domains also associate through a hydrophobic interaction network with the top part of M2 at Tyr^{122} and Leu^{119}, the compact Tyr^{122}-hydrophobic cluster (or the loose cluster, see more in supplemental Fig. S5 and the following section). These motions and changes in domain organization are definitively monitored by the changes in the resistance against trypsin at the tryptic T2 site Arg^{198} on the Val^{200} loop and against proteinase K (prtK) at the major cleavage sites Leu^{119} on the top part of M2 and at Thr^{242} on the A/M3-linker as demonstrated previously (23, 24) and as noted below.

Arg^{198}: the association of the largely rotated A domain with the P domain at the Val^{200} loop by ionic and hydrogen bonding interactions involving Arg^{198} is explicitly monitored by the complete resistance of Arg^{198} against the tryptic attack.

Leu^{119}: formation of the interactions involving Leu^{119} and Tyr^{122} on the top part of M2 are clearly monitored by the complete resistance at Leu^{119} against prtK attack. In $E1PCa_2$, Tyr^{122}-Leu^{119} on the top part of M2 is in van der Waals contact with the top of M4. In *E*2P, Tyr^{122}/Leu^{119} on M2 engages in the hydrophobic interaction network with the A and P domains. Thus both in the $E1PCa_2$ and *E*2P states, Leu^{119} is completely resistant against prtK attack. Then note that in order to realize the *E*2P structure from $E1PCa_2$, M2 (Tyr^{122}/Leu^{119}) should move away from its contact with M4, and largely incline to the A and P domains to produce the interaction at Tyr^{122}/Leu^{119}. Therefore in the intermediate transient state during $E1PCa_2 \rightarrow E2P + 2Ca^{2+}$, Leu^{119} becomes sterically available to prtK attack (as actually found in the transient state $E2PCa_2$ and $E2Ca_2{\cdot}BeF_3^-$ stabilized by the elongation of the A/M1'-linker).

Thr^{242}: Upon ATP binding and $E1PCa_2$ formation (as seen in the change $E1Ca_2 \rightarrow E1Ca_2{\cdot}CaAMPPCP/E1Ca_2{\cdot}AlF_4^-{\cdot}ADP$), the A domain rotates perpendicularly to the membrane plane thereby raising its junction with the A/M3-linker (as well as with the A/M1'-linker) and imposing a strain on this A/M3-linker (18). This change apparently causes complete resistance of Thr^{242} on the A/M3-linker against the prtK attack (18, 19, 24, 27). The strain of the A/M3-linker has been predicted to function as a motive force of the large A-domain's rotation parallel to membrane for the *E*1P to *E*2P isomerization (18, 19, 50, 51).

Results and Conclusion :

Shown in supplemental Fig. S3 and Table S1 are the proteolytic patterns and the approximate cleavage rates and resistance at Arg^{198} (producing A1 fragment) and at Leu^{119} and Thr^{242} (producing p95 and p81/83 fragments, respectively). In $E2Ca_2{\cdot}BeF_3^-$ and $E2PCa_2$, the tryptic T2 site Arg^{198} is completely resistant as in $E2{\cdot}BeF_3^-$ and *E*2P. On the other hand, the prtK site Leu^{119} in $E2Ca_2{\cdot}BeF_3^-$ and $E2PCa_2$ is rapidly cleaved, in sharp contrast to its complete resistance in $E1Ca_2{\cdot}BeF_3^-/E1PCa_2$ and $E2{\cdot}BeF_3^-/E2P$. The results reveal that in $E2Ca_2{\cdot}BeF_3^-$ and $E2PCa_2$, the A domain has already largely rotated from the position in $E1Ca_2{\cdot}BeF_3^-/E1PCa_2$ and docked onto the P domain at the Val^{200} loop (and at $TGES^{184}$) as in $E2{\cdot}BeF_3^-/E2P$, and that Leu^{119}/Tyr^{122} on the top part of M2 has been released from its contact with M4 in $E1Ca_2{\cdot}BeF_3^-/E1PCa_2$ but not yet reached a position to produce the interaction network at Leu^{119}/Tyr^{122} with the A and P domains (Tyr^{122}-hydrophobic cluster) in the $E2{\cdot}BeF_3^-/E2P$. Thus the structure of $E2Ca_2{\cdot}BeF_3^-$ and $E2PCa_2$ is intermediate between those of $E1Ca_2{\cdot}BeF_3^-/E1PCa_2$ and $E2{\cdot}BeF_3^-/E2P$.

It is concluded that in the transient $E2PCa_2$ state and its analog $E2Ca_2{\cdot}BeF_3^-$ stabilized by elongation of the A/M1'-linker, the inclining motions of M2 and the A and P domains have not yet advanced enough to gather and form the interaction network around Leu^{119}/Tyr^{122}. Actually, formation of this interaction network has been shown to be critical for Ca^{2+} release and formation of the Ca^{2+}-released *E*2P ground state by mutations of each of the seven residues involved in the network, Tyr^{122}-hydrophobic cluster (11-13). The results also reveal the critical role of the native length of A/M1'-linker for inducing the inclining motions of the A and P domains and M2 to deocclude and release Ca^{2+} from $E2PCa_2$ and to produce the *E*2P ground state structure.

Regarding $E1Ca_2{\cdot}BeF_3^-$ of wild type ($E1PCa_2{\cdot}Mg$ analog), it should be mentioned that the T2 site Arg^{198} is cleaved more slowly than in $E1Ca_2{\cdot}AlF_4^-{\cdot}ADP$ and $E1Ca_2{\cdot}AlF_x$ (the transition state analogs of

phosphorylation) as demonstrated previously (27). This indicates that during $E1PCa_2{\cdot}Mg$ formation from the transition state, the A domain likely rotates to some extent parallel to the membrane plane and brings Arg^{198} close to the P domain (although this change is obviously not enough to reach the $E2PCa_2$ and $E2P$ states, *i.e.* for the change $E1PCa_2 \rightarrow E2PCa_2 \rightarrow E2P + 2Ca^{2+}$, the A domain should further rotate to produce its association with the P domain at Arg^{198}) (27). Interestingly, the T2 site cleavage rate in $E1Ca_2{\cdot}AlF_x$ of the elongated A/M1'-linker mutant is between those of the wild-type $E1Ca_2{\cdot}AlF_4^-{\cdot}ADP$/$E1Ca_2{\cdot}AlF_x$ and $E1Ca_2{\cdot}BeF_3^-$. The result indicates that elongation of the A/M1'-linker allows some rotation of the A domain, thereby bringing the structure of mutant $E1Ca_2{\cdot}AlF_x$ close (but not completely) to that of the wild-type $E1Ca_2{\cdot}BeF_3^-$ (see more in "DISCUSSION").

Proteolytic Structural Analysis of $E2Ca_2{\cdot}BeF_3^-$ Formed from $E2{\cdot}BeF_3^-$ and Ca^{2+}

— for supplemental Fig. S4 and Table S2 —

The effect of high concentration 10 mM of Ca^{2+} in the presence of A23187 on the structure of $E2{\cdot}BeF_3^-$, $E2{\cdot}AlF_4^-$, and $E2{\cdot}MgF_4^{2-}$ were examined by proteolysis. In the A/M1'-linker elongated mutant, Ca^{2+}-treatment of $E2{\cdot}BeF_3^-$ results in exactly the same proteolytic pattern as for $E2Ca_2{\cdot}BeF_3^-$ formed from $E1Ca_2$ and BeF_x. The results show that the stable $E2Ca_2{\cdot}BeF_3^-$ is produced from $E2{\cdot}BeF_3^-$ most probably by lumenal Ca^{2+} binding to the transport sites (mimicking $E2P + 2Ca^{2+} \rightarrow E2PCa_2$).

In wild type, the $E2{\cdot}BeF_3^-$ complex is destroyed by 10 mM Ca^{2+} and converted to $E1Ca_2$. This is probably by the conversion $E2{\cdot}BeF_3^- + 2Ca^{2+} \rightarrow E1Ca_2{\cdot}BeF_3^-$ (mimicking lumenal Ca^{2+}-induced reverse conversion $E2P + 2Ca^{2+} \rightarrow E1PCa_2$) and by the subsequent Ca^{2+} substitution of Mg^{2+} at the catalytic site in $E1Ca_2{\cdot}BeF_3^-$ as shown previously (27).

$E2{\cdot}AlF_4^-$ and $E2{\cdot}MgF_4^{2-}$ complexes of the mutant and wild type are also destroyed by 10 mM Ca^{2+} resulting in $E1Ca_2$. This is probably because Ca^{2+} at such a high concentration disrupts the closed gate, *i.e.* the closed structure of the Ca^{2+}-releasing pathway in the transmembrane and lumenal regions, and consequently disorganizes the AlF_4^-- and MgF_4^{2-}-ligations at the catalytic site as described previously (27).

Supplemental Figure S5.
Interaction network around Leu^{119}/Tyr^{122} on M2 with the A, P, and N domains in *E*2P analogs.
The crystal structures *E*1Ca$_2$·AlF$_4^-$·ADP, *E*2·BeF$_3^-$, *E*2·BeF$_3^-$(TG) are depicted as in Fig. 2 (PDB accession code 1T5T (17), 2ZBE (21), and 2ZBF (21), respectively). *Upper panels*, whole molecules; *lower panels*, regions of the seven hydrophobic residues involved in the Tyr^{122}-hydrophobic cluster in *E*2·BeF$_3^-$(TG) (*Y^{122}-HC*, *semitransparent green sphere*). These seven residues are Leu^{119}/Tyr^{122} on the top part of M2, Ile^{179}/Leu^{180}/Ile^{232} of the A domain, and Val^{705}/Val^{726} of the P domain. In *E*2·BeF$_3^-$(TG), the compact Tyr^{122}-hydrophobic cluster is fully achieved. On the other hand, *E*2·BeF$_3^-$ crystallized without TG possesses a rather loose cluster (Ile^{179}/Leu^{180}/Ile^{232} and Val^{705}/Val^{726}, *semitransparent blue sphere*) and a more extended interaction network (*dashed green line circle*) involving Leu^{119} and Lys^{120} next to Leu^{119}/Tyr^{122} (*semitransparent pink sphere*). See more in the following analysis of the structure and role of the interaction network.

Hydrophobic Interactions at Tyr^{122} for E2P Ground State: Fully Realized Compact Tyr^{122}-hydrophobic Cluster or Rather Loose Cluster?

In the crystal structure *E*2·BeF$_3^-$(TG) as well as in *E*2·AlF$_4^-$(TG), *E*2·MgF$_4^{2-}$(TG), and *E*2·AlF$_4^-$·AMPPCP without TG, the Tyr^{122}-hydrophobic cluster is fully formed by the seven residues on the top part of M2 and the A and P domains. In *E*2·BeF$_3^-$ crystallized without TG (2ZBE (21) and 3B9B (22)), the side chains of Leu^{119} and Tyr^{122} are peripheral to and oriented outward from the other five clustered residues (Ile^{179}/Leu^{180}/Ile^{232} and Val^{705}/Val^{726}), and Leu^{119} is in close contact with Thr^{430} on the N domain (2ZBE). Also in *E*2·BeF$_3^-$ without TG, Lys^{120} next to Leu^{119}/Tyr^{122} is now facing the P domain and in close contact with Gly^{723}/Ser^{722}/Lys^{728} in the immediate vicinity of Val^{726} of the hydrophobic cluster. Thus, *E*2·BeF$_3^-$ crystallized without TG possesses a rather loose cluster but has a more extended interaction network around Leu^{119}/Tyr^{122}. The inaccessibility of the prtK-site Leu^{119} (completely resistant) both in TG-free *E*2·BeF$_3^-$ (the Ca^{2+}-released *E*2P) and in *E*2·BeF$_3^-$ with bound TG (Refs. 23-25, also supplemental Figs. S3 and S4) may be reasonably accounted for by its steric protection seen in the crystal structures.

Our biochemical studies in solution (25) demonstrated that TG binding to *E*2·BeF$_3^-$ closes the lumenal gate from an open state, as in fact seen in the crystal structural change accompanying *E*2·BeF$_3^-$ → *E*2·BeF$_3^-$(TG) (21). *E*2·AlF$_4^-$, the transition state analog of *E*2P hydrolysis, was also demonstrated in solution to have a closed lumenal gate in contrast to the open one in *E*2·BeF$_3^-$, the *E*2P ground state analog (25). Therefore according to the crystals *E*2·BeF$_3^-$ and *E*2·BeF$_3^-$(TG), the compact Tyr^{122}-hydrophobic cluster is expected to be fully formed together with lumenal gate closure during the reaction from *E*2P ground state to the transition state of *E*2P hydrolysis.

On the other hand, we found by mutation and kinetic studies of each of the seven residues involved in the Tyr^{122}-hydrophobic cluster (11-13) that all the seven residues are critical for Ca^{2+} release from the transient *E*2PCa$_2$ state and for *E*2P hydrolysis, therefore probably for formation of the Ca^{2+}-free *E*2P ground state structure. Actually, mutation of Tyr^{122} and Leu^{119} among the seven residues caused the most severe functional defect, indicating that they play central roles in the interaction network (13). Our preferred view from these findings is rather that, under physiological (not crystallizing) conditions, a full and compact Tyr^{122}-hydrophobic cluster is required for (*i.e.* present in) the *E*2P ground state structure, which possesses the lumenally opened Ca^{2+} release pathway and the catalytic site with hydrolytic function (11-13). This view seemingly conflicts with the atomic structure of *E*2·BeF$_3^-$ (although this prediction was made before the *E*2·BeF$_3^-$ crystal structure was solved).

An important question for us now is whether the Tyr^{122}-hydrophobic cluster should be fully formed by all seven residues under physiological (not crystallizing) conditions to realize the *E*2P ground state, or is a loose cluster with an extended interaction network around Tyr^{122} (seen in the *E*2·BeF$_3^-$ crystal) sufficient to stabilize this state. A compromise would be that the gathering of all seven residues in the Tyr^{122}-hydrophobic cluster occurs in some ordered sequence and not necessarily all at once. In fact, mutation of each of the seven residues exhibited different degrees of functional inhibition (see more detailed discussion in Ref. 13).

Nevertheless, we should take into account possible structural perturbations by agents used for stabilizing the transmembrane helices during crystallization of *E*2·BeF$_3^-$ with the lumenal Ca^{2+}-release pathway open (gate). For example, in the structure of *E*2·BeF$_3^-$ crystallized without TG, Mg^{2+} is bound at or near Glu^{309} (the Ca^{2+} binding site II) because of the very high concentration of Mg^{2+} used (50 mM, 3B9B (22)), or a low pH could protonate the Ca^{2+} ligands (pH 5.7, 2ZBE (21)). The transmembrane structures stabilized in these ways might possibly differ from those in the absence of such agents.

To expand on these examples, let us assume that a fully formed and compact Tyr^{122}-hydrophobic cluster is required for stabilizing the Ca^{2+}-free sites in the *E*2P ground state. The cluster in *E*2·BeF_3^- crystallized in Mg^{2+} is possibly disrupted by the Mg^{2+} binding at or near the transport site, as also could occur by lumenal Ca^{2+} binding to *E*2·BeF_3^- (*E*2P) to produce *E*2Ca_2·BeF_3^- (*E*2PCa_2). It is possible that the structure of Mg^{2+}-bound *E*2·BeF_3^- is somewhat between that of the *E*2PCa_2 transient state and that of the *E*2P ground state, as possibly in *E*2P with bound (but not occluded) Ca^{2+} within the open release pathway. If this is the case, the crystal structure of Mg^{2+}-bound *E*2·BeF_3^- may suggest that the Tyr^{122}-hydrophobic cluster is only fully formed on Ca^{2+} release and appearance of the *E*2P ground state with empty transport sites.

It is also possible that *E*2·BeF_3^- crystallized at low pH (with likely protonation of transport sites and open lumenal gate *i.e.* un-occluded protons) may rather reflect an *E*2P ground state after protonation of the transport sites but before gate-closure. Closure of the gate is achieved subsequently in the transition state with occlusion of the protons (25). This view agrees with the predicted proton-counter transport mechanism, in which protonation occurs in the *E*2P ground state (*e.g.* see Scheme 2 in Ref. 56). In this case, the structure *E*2·BeF_3^- crystallized at the low pH may suggest that the compact Tyr^{122}-hydrophobic cluster becomes loose by the protonation in the *E*2P ground state. Actually, the cluster (either full and compact or loose) formed in the *E*2P ground state is disassembled or becomes very loose upon *E*2P hydrolysis to *E*2 (as demonstrated by the very rapid prtK-cleavage at Leu^{119} in *E*2 (Ref. 23, and see Supplemental Figs. S3 and S4)).

In the two types of crystals *E*2·BeF_3^- formed with Mg^{2+} or with low pH, it is interesting to note that the lumenal gate is much more widely opened with Mg^{2+} than with the likely protonation at the low pH. Taking into account these possible interpretations of the two types of *E*2·BeF_3^- crystals, it is tempting to speculate that the successive structural changes for gate opening to release Ca^{2+} (*E*2PCa_2 → *E*2P + 2Ca^{2+}), protonation of the empty sites in the *E*2P ground state, and the subsequent gate closure to occlude protons and to prevent Ca^{2+} leakage may possibly be described by the following changes. Namely, *E*2Ca_2·BeF_3^- with a closed gate (*E*2PCa_2 with the occluded two Ca^{2+}) → *E*2·BeF_3^- with an open gate crystallized with Mg^{2+} (possibly similar to *E*2P with un-occluded Ca^{2+} immediately before Ca^{2+} release) → *E*2·BeF_3^- with an open gate without any ligation (the genuine *E*2P ground state after Ca^{2+} release, *i.e.* with empty transport sites) → *E*2·BeF_3^- with an open gate crystallized at the low pH (*E*2P with the protonated transport sites before closing gate) → *E*2·AlF_4^- with closed gate (the transition state of *E*2P hydrolysis, with occluded protons).

Roles of A/M1'-linker and Interaction Network at Tyr^{122} in Ca^{2+}-release from E2PCa_2

What our present and previous studies clearly reveal is that the A/M1'-linker and its strain in *E*2PCa_2, is critical for Ca^{2+}-deocclusion/release from the transient *E*2PCa_2 state thereby producing the Ca^{2+}-free *E*2P ground state. This is accomplished probably by inducing the inclining motions of the A and P domains and connected helices M2/M1 and M4/M5 (Fig. 2 and supplemental Figs. S5 and S6). Such movements are reflected in the changes in resistance of Leu^{119} at the top part of M2 against prtK and of the tryptic T2 site Arg^{198} on the Val^{200} loop, showing that the structure of *E*2Ca_2·BeF_3^- (*E*2PCa_2) is intermediate between those of *E*1Ca_2·BeF_3^- (*E*1PCa_2) and the Ca^{2+}-free *E*2·BeF_3^- (*E*2P). The Ca^{2+}-free *E*2P ground state with the lumenal gate open is stabilized by the interaction network around Tyr^{122} (either by the fully produced compact Tyr^{122}-hydrophobic cluster or by the loose cluster with extended interaction network around Leu^{119}/Tyr^{122}).

Fig. S5

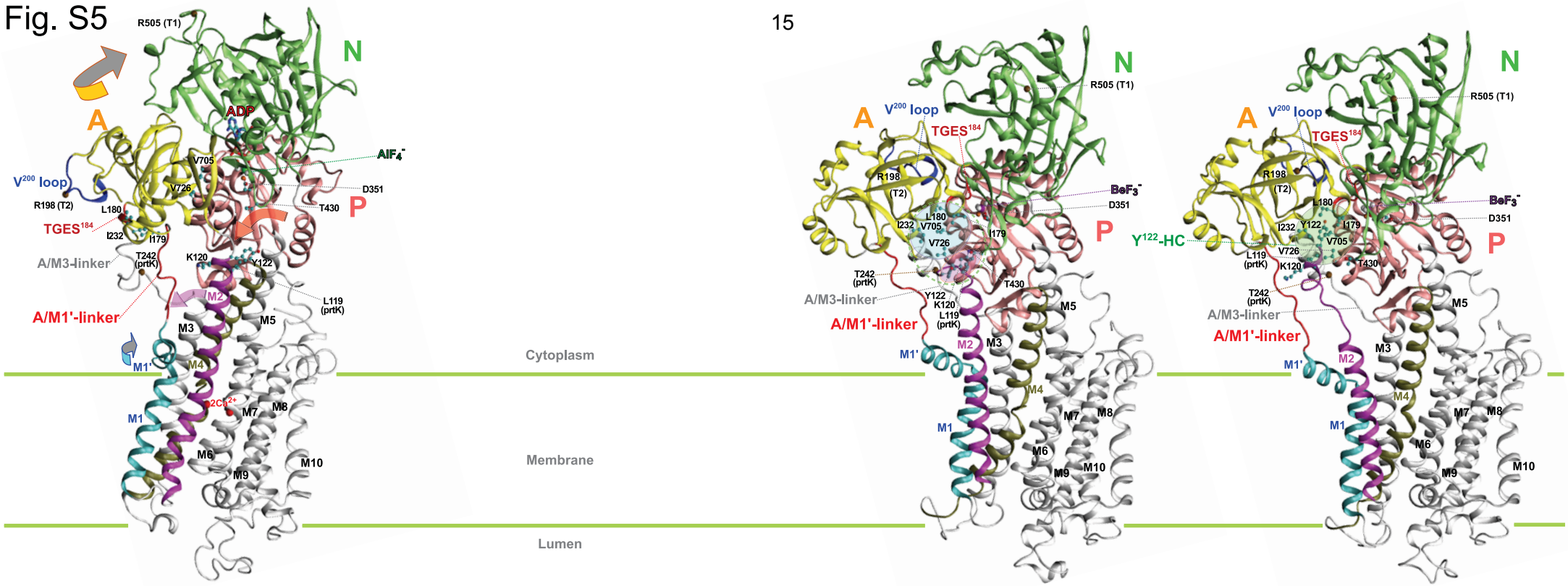

$E1PCa_2{\cdot}ADP{\cdot}Mg^{\ddagger}$ ($E1Ca_2{\cdot}AlF_4^-{\cdot}ADP$) ⇨ $E1PCa_2{\cdot}Mg$ ($E1Ca_2{\cdot}BeF_3^-$) ⇨ **$E2PCa_2{\cdot}Mg$ ($E2Ca_2{\cdot}BeF_3^-$)** ⇨ $E2P{\cdot}Mg$ ($E2{\cdot}BeF_3^-$) $E2P{\cdot}Mg$ ($E2{\cdot}BeF_3^-$(TG))

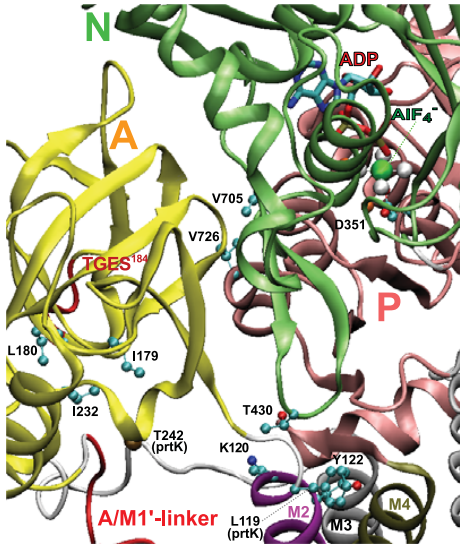

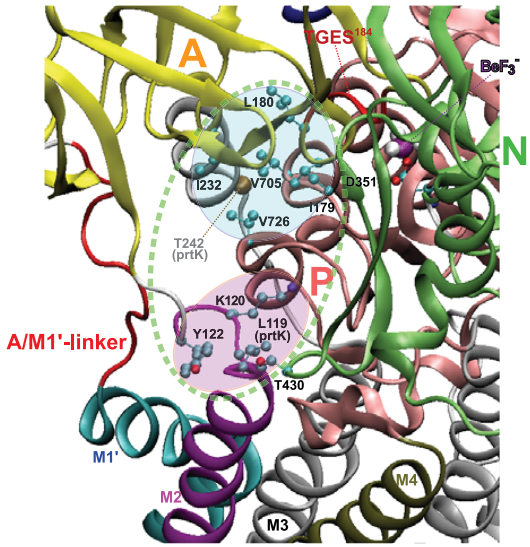

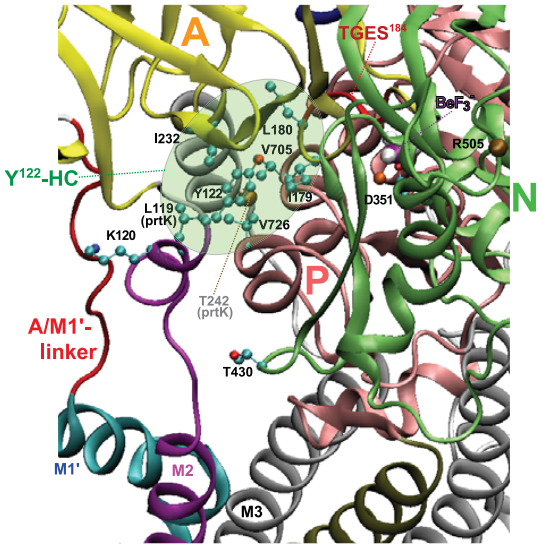

Supplemental Figure S6.

A cartoon illustrating the structural changes of the Ca^{2+}-ATPase and the predicted functional role of the A/M1'-linker during *E*P processing and Ca^{2+} release.

The schematic model was constructed on the basis of the mutation and kinetic studies of the A/M1'-linker (this study and Refs. 14 and 26) and Tyr^{122}-hydrophobic cluster (11-13), the proteolytic analyses (this study and Refs. 14, 23-25, and 27), and the crystal structures noted in the parentheses in the Figure. The *large curved arrows* indicate the approximate motions of the A domain (A), the A domain together with the P domain (A-P), M2, and M1' to realize the next structural state. The tryptic T2 site Arg^{198} (*198*) and prtK-sites Leu^{119} (*119*) and Thr^{242} (*242*) are indicated in each of the intermediates with (→) for rapid cleavage, (⋯→) for slow cleavage, and (→▮) for complete resistance. Note that the A/M1'-linker is strained in *E*2PCa_2 and the strain induces the inclinations of the A and P domains (A-P), M4/M5, and M2 to release Ca^{2+} and to realize the Ca^{2+}-released *E*2P. The structural models of *E*2, *E*1Ca_2, and *E*1PCa_2·ADP·$Mg^{‡}$ (the transition state of phosphorylation) are smaller in size to show the whole transport cycle.

Fig. S6

Proteolysis sites
- 198 tryptic T2 site (Arg[198])
- 119 prtK site (Leu[119])
- 242 prtK site (Thr[242])

Cleavage rate by proteolysis
- rapid cleavage
- slow cleavage
- complete resistance